DESIGN PROCEDURE OF 48V IN-WHEEL OUTER ROTOR SPMS FOR FULLY ELECTRIC VEHICLES

Xi-yun Ma*, Xiao-yan Wang, Juliette Soulard

WMG, University of Warwick, CV4 7AL Coventry, United Kingdom.
**xiyun.ma@warwick.ac.uk*
Keywords: COST MODELLING, ELECTRIC VEHICLE, IN-WHEEL, OUTER ROTOR PM MACHINE, 48V.

Abstract

This paper proposes a design procedure of 48V in-wheel outer rotor motors for fully electric vehicles. A case study with outer-rotor surface-mounted permanent-magnet motors (SPMs) adopted in Nissan Leaf vehicle with HYZEM urban drive cycle comprehensively illustrate vehicle simulations, motor and inverter designs, cooling design and drive cycle thermal investigation. Comparison between air and liquid cooling methods is also included. In addition, different manufacturing processes of the proposed outer-rotor SPM are considered during cost modelling and a strip layout factor is defined by analytical equations to account for electrical steel scrap. Accordingly, a recommendation is given with regards to minimising waste materials during the manufacturing process.

1. Introduction

The utilization of in-wheel direct drive motors in electric vehicle propulsion system is increasingly attractive due to independent control of each wheel leading to greater controllability and increased space in the cabin [1]. Mounting the motor in the rim of the wheel simplifies the mechanical layout and removing of the geared transmission and mechanical differential is beneficial in terms of weight and associated energy loss. However, the challenge lies in the limited space available for the motor in the wheel while high torque is required for the direct-drive operation. In addition, in-wheel motors have struggled for many years to gain a foothold in traditional automotive application due to unsprung mass, sealing for hash environment and system cost [2].

Electric vehicle manufacturers are starting to adopt 48V electrical systems allowing economical implementation while maintaining power output [3]. However, the low system voltage brings technical challenges in both motor design and inverter sizing. For example, the motor base speed and number of turns in the stator windings are constrained by the low voltage which also limits options for power electronic devices [4].

This paper proposes a design procedure for 48V, in-wheel direct-drive systems for electric vehicles integrating thermal modelling of both motor and inverter, and manufacturing process analysis of the motor to estimate machine cost. With consideration of the limited space for in-wheel application, both axial- and radial-flux machines were introduced in the literature [2, 5-11]. Fig. 1 summaries several machines with suitable size for in-wheel application, where machine type (radial/axial flux (RF/AF) with surface mounted/ interior PM (SPM/IPM), continuous torque density, and cooling method have been marked. Due to high torque density and low rotating speed, the radial-flux outer-rotor surface-mounted PM machine (SPM) has been selected to demonstrate the design procedure in this paper.

A case study with an electric vehicle powertrain and urban drive cycle is presented in section 2. It is worth mentioning that the design approach can be used for any type of vehicle, drive cycle or motor. The key aspects of the design process include vehicle simulation, motor and inverter designs, cooling design and drive cycle thermal simulation, as detailed in Section 3. In addition, different manufacturing processes are investigated and compared for the proposed outer rotor SPM in Section 4.

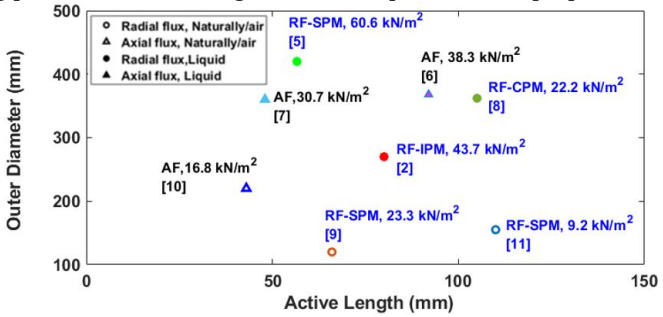

Fig. 1 Selection of electric machines with reasonable size for in-wheel application from the literature. Machine type, torque density and cooling method have been marked.. AF: axial flux SPM. RF: radial flux outer-rotor PM machine. CPM: consequent pole PM machine. IPM: interior PM machine. [2, 5-11]

2. Design Procedure

The proposed design procedure to address the challenges of the task is shown in Fig. 2. For illustration purpose, Nissan Leaf vehicle with HYZEM urban drive cycle has been selected as the case study. Given the vehicle specification and drive cycle data (see TABLE 1), the torque demand of the whole vehicle is calculated with the consideration of different payloads and different road conditions (with or without gradient during the drive cycle).

Both 2-wheel and 4-wheel drives can be employed for a fully electric vehicle. The torque demand for each motor in a 2-wheel system is double for value for a 4-wheel system. For the same machine topology and size, higher electric loading and magnetic loadings are necessary for the higher torque

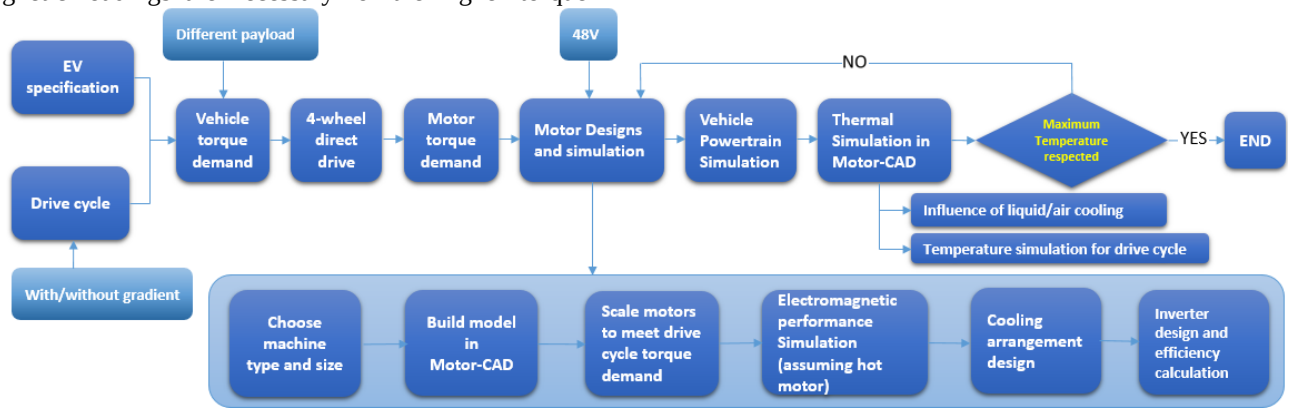

Fig. 2 Design procedure for 48V in-wheel motors in fully electric vehicles.

demand in the case of a 2-wheel drive, which requires a careful machine cooling design and thermal management. On the other hand, 4-wheel drive system has higher unsprung mass and higher cost of the motors (assuming the same motor size as a 2-wheel drive is used). Therefore, a tool allowing to analyse the 2 solutions is greatly helpful to decide on most suitable drive train characteristics.

The 4-wheel drive is selected for illustration of the simulation of the motor, powertrain and thermal performance. Since both the motor and inverter losses are affected by temperature, it is desirable to simulate the component temperatures and dynamically update their losses during a real-time drive cycle simulation. However, this involves computational complexity. With the proper design, it was found out that the average efficiency over the drive cycle did not vary significantly with temperature of motor or power electronics devices for the considered case. As a result, the drive cycle thermal modelling can be performed 'offline' in Motor-CAD using the motor losses obtained at the highest acceptable operating temperature. This approach significantly reduces the computation burden without compromising the accuracy of the energy consumption per cycle, leading to the design process in Fig. 2. The effect of air and liquid cooling methods can then be investigated as a part in the procedure.

TABLE 1 Nissan Leaf vehicle specification and HYZEM data

Vehicle weight (kg)	1580	Frontal area (m^2)	2.29
Rolling resistance coefficient	0.007	Wheel radius (m)	0.203
Drag coefficient	0.28	Maximum payload (kg)	450
Total distance (m)	3476	Average speed (km/h)	22.3
Total time (s)	560	Maximum speed (km/h)	56.53

3. Case Study

3.1. Vehicle Torque Demand

According to the vehicle specification of Nissan Leaf and the drive cycle data of HYZEM in TABLE 1 [12], the torque demand of the vehicle can be calculated as the production of total tractive effort of the vehicle required for the expected speed [13] and the effective tyre radius. Fig. 3 illustrates the influence of different payloads and gradient conditions on vehicle peak torque and peak power demands. The gradient is assumed to be adopted for the whole drive cycle. Without payload and under road condition with 0° gradient, the vehicle peak torque and power demand are 726 Nm and 24 kW. However, with a maximum payload of 450 kg of Nissan Leaf (proximately 3-4 passengers and a driver), and assuming 0° gradient, the vehicle peak torque and power demands are 933 Nm and 31 kW, respectively. While, with consideration of a gradient of 5°, the vehicle demands dramatically increase to 1274 Nm and 51 kW, respectively. The increment are 36.5% in torque and 64.5% in power compared with 0° gradient condition.

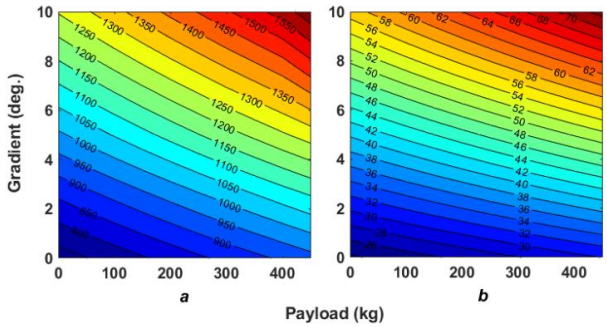

Fig. 3 Influence of payload and gradient conditions on vehicle demands.
(a) Peak vehicle torque demand in Nm.
(b) Peak vehicle power demand in kW.

3.2. Motor Designs and Simulation

Fractional-slot PM machine with non-overlapping winding is adopted in this paper due to the advantages such as high power density, high fault-tolerant capability, combined with short end-windings and low torque ripple [14, 15]. Fig. 4 shows the cross-section of the 3-phase, 54-slot/48-pole outer rotor SPM. A fundamental winding factor of 0.945 is achieved by double-layer concentrated winding.

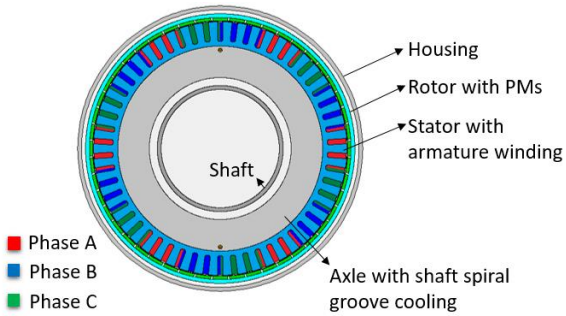

Fig. 4 Cross-section of the 3-phase, 54-slot/48-pole outer rotor SPM with fractional-slot, double layer concentrated winding.

In order to achieve the torque demand, the machine should be designed with proper outer diameter and active length within the size constraint, according to:

$$T = \frac{\pi}{2} D^2 L B Q \tag{1}$$

where D is airgap diameter (in m), L is active length (in m), B is magnetic loading (in T) and Q is electrical loading (in A/m). In addition, as an important design parameter, the optimal split ratio between rotor and stator outer diameters can be derived according to [16].

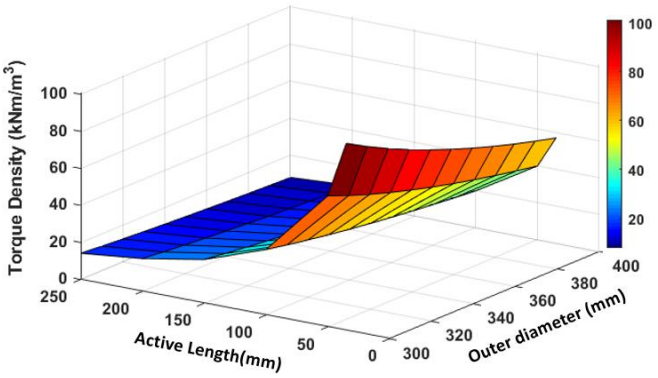

Fig. 5 Influence of machine size on the torque density, at $T = 250$ Nm.

For a 4-wheel system, the torque demand of each motor is calculated by the total vehicle torque demand divided by 4. As a result, the motor torque of 250 Nm is selected as the design target with regard to the 933 Nm vehicle torque demand for 0° gradient road condition as mentioned previously. Fig. 5 illustrates the influence of machine outer diameter and active length on the torque density. It is apparent that the highest torque density in Fig. 5 is at $101\ \mathrm{kN/m^2}$ with the smallest motor size ($35\ \mathrm{mm} \times 300\ \mathrm{mm}$). Although lighter motor weight can be beneficial to unsprung mass, the higher electrical and magnetic loadings require a careful machine cooling design. In this paper, the rotor outer diameter is fixed at 340 mm for the 16" Nissan Leaf wheel on the basis of mechanical arrangement of the in-wheel outer-rotor SPM. For this size, the torque density can be decreased

from 79 kN/m^2 to 11 kN/m^2 by increasing active length. However, a shorter axial length would be more desirable for in-wheel applications.

TABLE 2 Motor specifications for a 4-wheel in-wheel Nissan Leaf with HYZEM drive cycle

Slot number	54	Shaft diameter (mm)	160
Pole number	48	Active length (mm)	40
Rotor outer diameter (mm)	340	DC bus voltage (V)	48
Airgap length (mm)	1	Current density (A/mm^2)	11
Stator outer diameter (mm)	322	Torque (Nm)	250
Axel diameter (mm)	260	Base speed (rpm)	340

As the demand of peak torque and peak power during the drive cycle occurred at different times, it is worth mentioning that an appropriate torque/speed is important to ensure that the motor operating region can cover all the operating points of the drive cycle (flux weakening capability). Additionally, design of the motor should provide a high efficiency region, matching where the majority of drive cycle operating points optimally. This indicates that the selection of motor type and optimization of the motor dimension should be considered based on the drive cycle. With consideration of both the electromagnetic and thermal performances, the motor is optimized for a 4-wheel Nissan Leaf with maximum payload and 0° gradient HYZEM drive cycle. The key parameters are listed in TABLE 2.

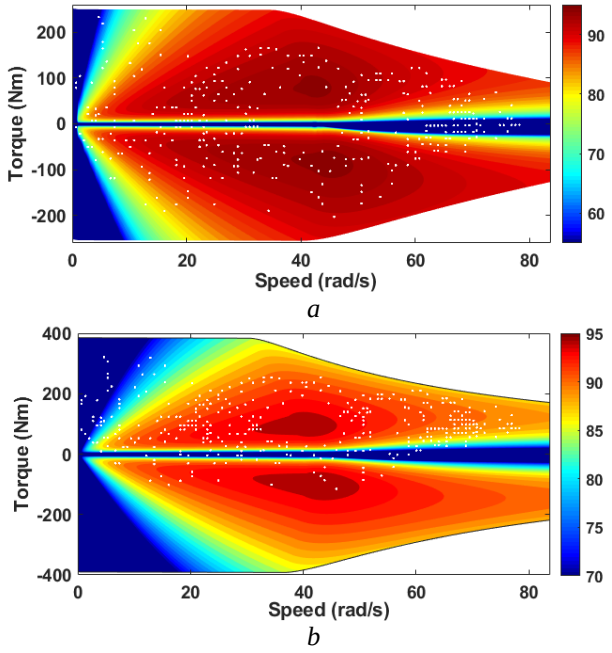

Fig. 6 Efficiency map of in-wheel outer rotor SPM with drive cycle operating points for 4-wheel direct drive application.
(a) Maximum payload and 0° gradient. $I_{max} = 260$ A, drive cycle average efficiency at 87%,
(b) Maximum payload and 5° gradient. $I_{max} = 400$ A, drive cycle average efficiency at 89%.

With consideration of flux-weakening limitation [4, 17], the efficiency map with superposed drive cycle operating points are shown in Fig. 6. All the drive cycle operating points are within motor working region. The initial design in Fig. 6 (a) was in accordance with the torque demand of the scenario with maximum payload and 0° gradient. The machine dimensions are kept the same as initial design, but the current varied for different scenarios as required by gradient and payload combinations. Based on energy use, average efficiency across the drive cycle is calculated and compared between different conditions.

3.3. Inverter Loss and Efficiency based on the Motor

Based on the 48V DC link voltage and the 400 A (peak) maximum current for maximum payload and 5° gradient, Semicron SK300MB080 MOSFET module has been chosen for the inverter design [18]. One module contains two MOSFETs, with integrated body diodes, constituting one leg of inverter. The inverter loss calculation includes switching and conduction losses of the MOSFET and integrated body diodes, on the basis of their characteristics and measured loss figures from the device datasheet [19, 20]. Key factors affecting inverter loss are addressed by the following assumptions:

i. The inverter has the same gate drive resistance and stray inductance as those used in the device manufacture tests for obtaining the datasheet characteristics, such as on/off losses of MOSFET, E_{on}/E_{off} and diode reverse recovery energy E_{rr}.

ii. Under linear modulation and with the switching frequency f_{sw} far greater than the fundamental frequency f_n, the inverter loss can be calculated analytically using a single current value. In this case study, the ratio between f_{sw} and f_n, is 24.

The MOSFET and diode switching losses, $P_{sw(M)}$ and $P_{sw(D)}$, respectively, are calculated using (2) and (3) [19].

$$P_{sw(M)=}\frac{\sqrt{2}f_{sw}\left(E_{on}+E_{off}\right)}{\pi}\times\frac{I_{out}}{I_{ref}}\times\left(\frac{V_{dc}}{V_{ref}}\right)^{K_v}\times\left[1+TC_{sw}\times\left(T_j-T_{ref}\right)\right] \quad (2)$$

$$P_{sw(D)=}\frac{\sqrt{2}f_{sw}E_{rr}}{\pi}\times\left(\frac{I_{out}}{I_{ref}}\right)^{k_i}\times\left(\frac{V_{dc}}{V_{ref}}\right)^{K_v}\times\left[1+TC_{Err}\times\left(T_j-T_{ref}\right)\right] \quad (3)$$

where I_{out} is the rms value of the output current, I_{ref}, V_{ref} and T_{ref} are reference values of the switching loss measurements taken from the datasheet, TC_{sw} and TC_{Err} are temperature coefficients of the switching losses of MOSFET and diode, T_j is device junction temperature, K_V and K_i are exponents for the voltage and current dependency of switching losses, V_{dc} is the DC link voltage.

The MOSFET and diode conduction losses,$P_{cond(M)}$ and $P_{cond(D)}$ are calculated using (4) and (5) [20].

$$P_{cond(M)}=R_{DS}\hat{I}_{out}^2\left(\frac{1}{8}+\frac{mcos(\varphi)}{3\pi}\right) \quad (4)$$

$$P_{cond(D)}=V_F\hat{I}_{out}\left(\frac{1}{2\pi}-\frac{mcos(\varphi)}{8}\right)+R_F\hat{I}_{out}^2\left(\frac{1}{8}-\frac{mcos(\varphi)}{3\pi}\right) \quad (5)$$

where $\hat{I}_{out}$ is peak value of output current, R_{DS} and R_F are MOFSFET drain source and diode on-state resistances, V_F is diode forward voltage, $\cos(\varphi)$ is motor power factor and m is modulation index, defined as $\frac{\hat{V}_{out}}{0.5V_{dc}}$ with $\hat{V}_{out}$ being peak value of output phase voltage.

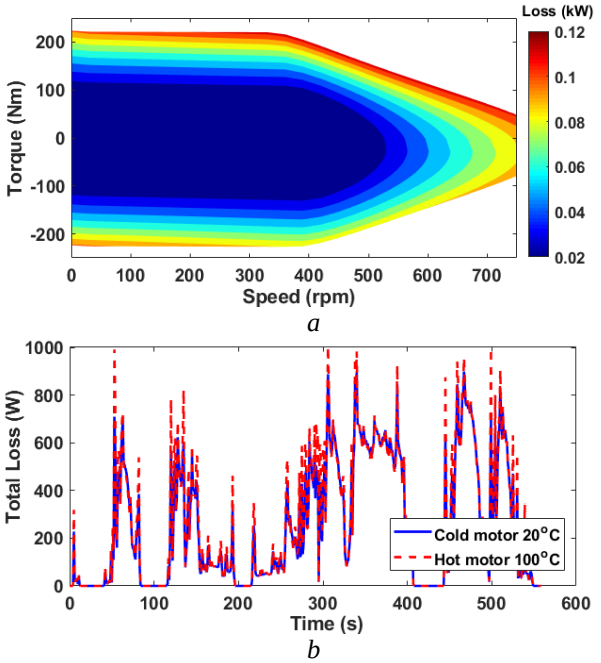

Fig. 7 Losses of the outer rotor SPM and inverter. $V_{dc}=48\,V,\ I_{max}=260\,A$.
(a) Total inverter loss based on the motor.
(b) Total loss during drive cycle, including motor and inverter losses.

Fig. 7 (a) shows the inverter loss map corresponding to the motor performance of maximum payload 450 kg and no gradient scenario. Accordingly, the inverter and motor total losses are obtained for the drive cycle, as shown in Fig. 7 (b).

According to the total losses, difference in efficiency of cold and warm electrical machines combined with power electronics devices are shown in TABLE 3. The average efficiency is calculated as the ratio of total output energy to total input energy. It can be seen that the influence of machine temperature on drive cycle efficiency is not significant. The inverter loss only has a minor affect on the system efficiency.

TABLE 3 Comparison of average drive cycle efficiency between cold and warm motors combined with or without power electronic devices

Machine temp.(℃)	Motor only (%)	Motor & inverter (%)	Input energy per cycle (J)
20	88	86	4079
100	87	85	4126

3.4. Cooling Design and Thermal Modelling

Shaft spiral groove cooling arrangement is selected for the outer rotor SPM, as shown in Fig. 4. Both air and liquid cooling methods are considered for the investigation of temperature variations in this paper. Therefore, the most appropriate cooling method can be selected for different scenarios and expected life time versus cost of the machine can be deduced.

EGW50/50 is used as the cooling fluid, which is a mix of ethylene glycol and water commonly used as a vehicle coolant. Fluid volume flow rate is 10 L/min. Inlet temperature is set at 65℃. In addition, active cooling only and no endcap cooling is considered. Natural convention is applied for housing outer cooling.

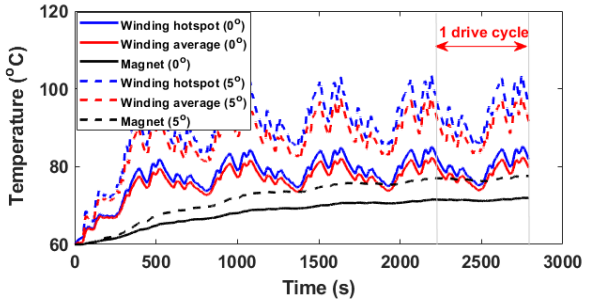

a

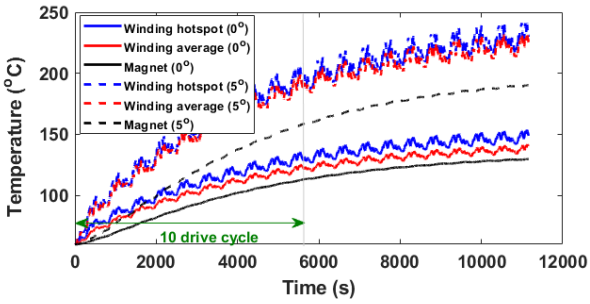

b

Fig. 8 Drive cycle thermal performance comparison between different cooling methods. Solid lines: maximum payload and 0° gradient. Dash lines: maximum payload and 5° gradient.
(a) Liquid cooling, (b) air cooling.

Based on the instantaneous copper loss, iron loss, and magnet loss of the electrical machines during the drive cycle, the thermal performance is simulated by Motor-CAD. The difference between air and liquid cooled is clearly demonstrated in Fig. 8, in terms of the temperature variation of winding and magnet. Additionally, both 0° and 5° gradient conditions have been investigated for several drive cycle periods. As a result, liquid cooling could be adopted for both scenarios with and without gradient (Fig. 8 (b)).Without gradient, air cooling only grants 3 hours (20 periods of the drive cycle) before the maximum temperature (140℃) is reached in the winding, as shown in Fig. 8 (b). It can also be found that the thermal steady-state is reached much faster with liquid cooling.

4. Manufacturing and Cost of Electrical Machines

For high volume production, a large proportion of the cost is linked to the electric machine material cost. TABLE 4 lists the material, weight and cost of different parts of the machine. While manufacturing the rotor and stator stacks, a significant portion of the electrical steel is scrap and this needs to be considered.

TABLE 4 Material, weight and cost of different parts in the machine

Component	Material	Weight (kg)	Active material cost (£)
Stator lamination	M350-50A	5.69	11.4
Rotor lamination	M350-50A	1.62	3.3
Magnet	N42SH	1.07	107
Winding	Copper	3.2	28.2
Shaft	Iron (Si 1%)	1.13	1.7
Axel	Alloy 195 Cast	8.176	24.6
Rotor banding	Fibre glass	0.05	-
Total incl. housing	--	28.45	176.2

Two methods are considered: one is punching the stator and rotor concentrically as shown in Fig. 9 (a), the other is punching the stator in segments of any angle and punching the whole rotor individually, see Fig. 9 (b). The specific case of a stator segment corresponding to one tooth allows a higher slot fill factor with precision winding and tooth tips for torque ripple

reduction. The scrap area of rotor and stator have been marked in different colours. The proposed analytical equations for scrap material volume of stator (V_{ss}) and rotor (V_{rs}) can be obtained on the basis of the scrap area in Fig. 9.

For punching stator and rotor concentrically, the rotor scrap material volume is given by

$$V_{rs} = L \times \left(x_1 x_2 - \frac{1}{4}\pi D_{ro}^2\right) \tag{6}$$

where L is motor active length, D_{ro} is rotor outer diameter. The difference between punching material edge and rotor outer diameter is assumed to be at least 3 times the thickness of lamination (W_{lam}), so that x_1 and x_2 in Fig. 9 (a) can be defined as

$$x_1 = D_{ro} + 2n \tag{7}$$

$$x_2 = D_{ro} + 2n \tag{8}$$

where $n \geq 3W_{lam}$.

The stator scrap material volume is given by

$$V_{ss} = L \times (\frac{1}{4}\pi D_1^2 - A_{stator}) \tag{9}$$

where A_{stator} is stator cross-section area, and the stator punching outer diameter is expressed as

$$D_1 = D_{so} + m, \qquad m \in [0, 2(l_g + l_m)] \tag{10}$$

where l_g is airgap length and l_m is magnet thickness.

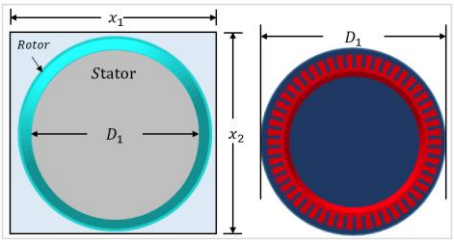

a

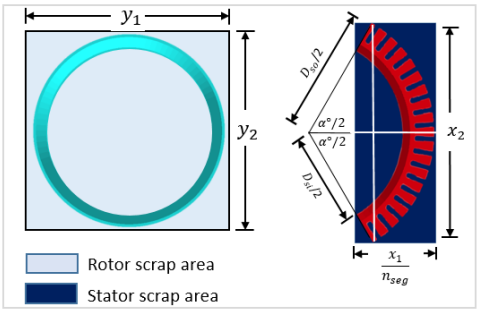

b

Fig. 9 Two manufacturing methods for stator and rotor of outer rotor machine.
(a) Punching stator and rotor concentrically.
(b) Punching stator and rotor individually.

For punching stator and rotor individually, the stator is manufactured in segments and α is the angle of each segment (see Fig. 9 (b)). Hence, number of segments is

$$n_{seg} = \frac{360°}{\alpha°} \tag{11}$$

The stator scrap material volume is given by

$$V_{ss} = L \times (x_1 x_2 - A_{stator}) \tag{12}$$

where

$$x_1 = n_{seg} \times \left(\frac{D_{so}}{2} - \frac{cos\left(\frac{\alpha°}{2}\right) D_{si}}{2} + 2n\right) \tag{13}$$

$$x_2 = D_{so}\, sin\frac{\alpha°}{2} + 2n \tag{14}$$

where D_{si} and D_{so} are stator inner and outer diameters.

Different from the stator, the rotor is punched as a whole part, and the scrap material volume is given by

$$V_{rs} = L \times (y_1 y_2 - A_{rotor}) \tag{15}$$

where A_{rotor} is rotor cross-section area. y_1 and y_2 are:

$$y_1 = D_{ro} + 2n \tag{16}$$

$$y_2 = D_{ro} + 2n \tag{17}$$

Similar to the assumption in previous punching method, n is equal or greater than $3W_{lam}$.

A strip layout factor (*F*) is defined as the total amount of scrap electrical steel divided by the amount used in the electrical machine. TABLE 5 compares the material scrap weight for the stator (W_{ss}) and rotor (W_{rs}) and lamination strip layout factor of the outer-rotor SPM between the two manufacturing methods. The lamination manufacturing with concentrically punching is more favourable in terms of electrical steel needs, to be balanced with the reduced slot fill factor value and different manufacturing cost of the winding and impregnation processes.

The total material cost consists of the cost of both scrap and used material, as well as a scrap selling price at most 10% of material cost per weight. Including steel scrap, the cost for concentrically punching method has been increased by 30% than models considering weight of active material in machine only since the outer-rotor PM machines are ring-like. A higher strip layout factor in individually punching method leads to a machine cost increment at least of 41%, with 54 segments and 6.7° for each segment.

TABLE 5 Comparison of material scrap weight and lamination strip layout factor

	Concentrically	Individually with different n_{seg}			
		2	3	6	54
W_{ss} (kg)	21.9	26.7	19.6	9.4	5.8
W_{rs} (kg)	8.0	34.5	34.5	34.5	34.5
W_{total_scrap} (kg)	29.9	61.2	54.1	44.0	40.3
F_{stator}	3.9	4.7	3.4	1.7	1.1
F_{rotor}	6.2	26.7	26.7	26.7	26.7
F_{total}	4.3	8.8	7.8	6.3	5.8

5. Conclusion

In this paper, the design procedure of a 48V in-wheel outer- rotor SPM in a fully electric vehicle was proposed and illustrated through a case study. The drive cycle demands with different load conditions impact were presented first. Losses and efficiency were then calculated for both the electrical machine and on-board power electronic devices, considering hot components, before analysing the thermal behaviour of the motor with its dedicated cooling system. Last but not least, the design procedure included a cost analysis based on material weight but also including consideration of the significant electrical steel scrap, with general analytical explanation presented.

6. References

[1] Rahman, K. M., Patel, N. R., Ward, T. G., et al.: 'Application of direct-drive wheel motor for fuel cell electric and hybrid electric vehicle propulsion system', *IEEE Trans. Ind. Appl.,* Sept. 2006, 42, (5), pp. 1185-1192.

[2] Rix, A. J., Kamper, M. J.: 'Radial-flux permanent-magnet hub drives: a comparison based on stator and rotor topologies', *IEEE Trans. Ind. Electron.,* Jun. 2012, 59, (6), pp. 2475-2483.

[3] '48V propulsion technologies', https://www.borgwarner.
com/technologies/highlight/48v-propulsion-technologies, accessed 20 Sept. 2019

[4] Soong, W. L., Miller, T. J. E.: 'Theoretical limitations to the field-weakening performance of the five classes of brushless synchronous AC motor drive', *6th Int. Conf. Electr. Machines and Drives*, Oxford, UK, 8-10 Sept. 1993, pp. 127-132.

[5] Ifedi, C. J., Mecrow, B. C., Widmer, J. D., et al.: 'A high torque density, direct drive in-wheel motor for electric vehicles', *6th PEMD*, Bristol, UK, 27-29 Mar. 2012, pp. 1-6.

[6] 'YASA 750R e-motor', https://www.yasa.com/wp-content/uploads/2018/01/YASA-750-Product-Sheet.pdf, accessed 1 Sept. 2019

[7] Caricchi, F., Capponi, F. G., Crescimbini, F., et al.: 'Experimental study on reducing cogging torque and no-load power loss in axial-flux permanent-magnet machines with slotted winding', *IEEE Trans. Ind. Appl.,* Jul. 2004, 40, (4), pp. 1066-1075.

[8] Chung, S. U., Moon, S. H., Kim, D. J., et al.: 'Development of a 20-pole–24-slot SPMSM with consequent pole rotor for in-wheel direct drive', *IEEE Trans. Ind. Electron.,* Aug. 2015, 63, (1), pp. 302-309.

[9] Wrobel, R., Mellor, P. H.: 'Design considerations of a direct drive brushless machine with concentrated windings', *IEEE Trans. Energy Convers.,* Mar. 2008, 23, (1), pp. 1-8.

[10] Caricchi, F., Crescimbini, F., Honorati, O., et al.: 'Compact wheel direct drive for EVs', *IEEE Ind. Appl. Mag.,* Nov./Dec. 1996, 2, (6), pp. 25-32.

[11] Deshpande, Y. B., Toliyat, H. A., Nair, S. S., et al.: ' High-torque-density single tooth-wound bar conductor permanent-magnet motor for electric two wheeler application', *IEEE Trans. Ind. Appl.,* May/Jun. 2015, 51, (3), pp. 2123-2135.

[12] Barlow, T. J., Latham, S., McCrae, I. S., et al.:'A reference book of driving cycles for use in the measurement of road vehicle emissions', (TRL limited, Jun. 2009), pp. 1-284.

[13] Ehsani, M., Gao, Y., Emadi, A.: 'Modern electric, hybrid electric, and fuel cell vehicles', (CRC Press, 2010, 2nd edn.)

[14] Bianchi, N., Pre, M. D., Grezzani, G., et al.: 'Design considerations on fractional-slot fault-tolerant synchronous motors', *IEEE Trans. Ind. Appl.,* Jul./Aug. 2006, 42, (4), pp. 997-1006.

[15] El-Refaie, A. M.: 'Fractional-slot concentrated-windings synchronous permanent magnet machines: opportunities and challenges', *IEEE Trans. Ind. Electron.,* Jan. 2010, 57, (1), pp. 107-121.

[16] Shen, Y., Zhu, Z. Q., Wu, L. J.: 'Analytical determination of optimal split ratio for overlapping and non-overlapping winding external rotor PM brushless machines', *IEMDC*, Niagara Falls, ON, Canada, 15-18 May 2011, pp. 41-46.
[17] Soong, W. L., Miller, T. J. E.: 'Field-weakening performance of brushless synchronous AC motor drives', *IEE Proc-Electr. Power Appl.*, Nov. 1994, vol. 141, no. 6, pp. 331-340.
[18] 'Datasheet-SK300MB080', https://www.semikron.com/
products/product-classes/mosfet-modules/detail/sk300mb080
-24920960.html, accessed 10 Sept. 2019
[19] Wintrich, A., Nicolai, U., Tursky, W., et al.: 'Application Manual Power Semiconductors', (SEMIKRON International GmbH, 2015, 2nd edn.)
[20] Graovac, D., Purschel, M., Kiep, A.: 'MOSFET power losses calculation using the datasheet parameters', (Infineon technologies AG, 2006, 1st edn.)